Challenges in automated 4D Point Cloud Generation for Glacier Calving Monitoring at high temporal Resolution

Laura Camila Duran Vergara[1], Xabier Blanch Gorriz[2], Bindusara Nagathihalli Lokesh[1], Anette Eltner[1]

[1] Institute of Photogrammetry and Remote Sensing, Dresden University of Technology, Germany - (laura_camila.duran_vergara, bindusara.nagathihalli_lokesh, anette.eltner)@tu-dresden.de
[2] Department of Civil and Environmental Engineering, Universitat Politècnica de Catalunya, Spain - xabier.blanch@upc.edu

Keywords: Multi-Epoch Multi-Imagery (MEMI) processing, alignment accuracy, computational efficiency, glacier calving monitoring, change detection.

Abstract

To robustly support glacier calving monitoring at high temporal resolution and enable future AI-based calving forecasts, this study presents an optimized Multi-Epoch Multi-Imagery (MEMI) strategy for automated 4D point cloud model generation. To date, the dataset comprises over 160,000 images acquired since December 2024 by an autonomous multi-camera system operating at $30\,\mathrm{min}$ intervals at Glacier Perito Moreno (GPM), Argentina. Despite high scene variability and harsh environmental conditions, the proposed MEMI workflow effectively addresses constraints imposed by continuous glacier motion and image degradation. The enhanced strategy aims to generate precise dense clouds with high alignment accuracy and computational efficiency, forming the basis for subsequent analysis of glacier front evolution. To achieve this, various parameter configurations are evaluated, including AI-based image masking and adaptive, optimized alignment-adjustment settings. Results from a representative eight-day subset show that variations in the tie point computation strategy lead to measurable differences in alignment-adjustment efficiency, with the best configuration being about 11 % faster than the least efficient one. By contrast, adaptive alignment-adjustment consistently improves alignment accuracy. Moreover, masking enhances both image quality checking and reconstruction quality, and, albeit modestly, improves pre-failure deformation analysis. Furthermore, daily seasonal responses to alignment are observed, as accuracy varies with solar illumination relative to the camera positions. Applying the optimal configuration to 260 MEMI projects in under $42\,\mathrm{h}$ produced 518 high-precision dense clouds and detected calving retreat magnitudes of up to $17.5\,\mathrm{m}$, demonstrating the robustness and scalability of the proposed MEMI strategy for high-temporal-resolution 4D point cloud generation.

1. Introduction

Up-to-date global glacier monitoring studies, as reported by (The GlaMBIE Team, 2025), provide temporal resolutions at annual, decadal, and monthly frequencies, with the most common measuring techniques including glaciological measurements, digital elevation model differencing, and altimetry and gravimetry measurements. However, this work further indicates that validating these global models requires high-quality local observations to better quantify and propagate uncertainties to regional scales. High-quality observations involve increasing both the spatial and temporal resolution, yet achieving high temporal resolution remains particularly challenging in harsh natural environments. In recent years, temporal resolution has been increased by installing local, autonomously powered multi-camera systems in different environmental scenarios. Such systems are capable of providing high spatial resolution and high-frequency observations (Blanch et al., 2023), which are suitable for automated 4D point cloud reconstruction, thereby enabling improved change analysis, where the fourth dimension represents temporal evolution (Anders et al., 2022, Ulm et al., 2025, Eltner et al., 2017).

Building upon these developments, this paper presents an automated multi-camera system, comprising eight RGB cameras, installed in front of the lake-terminating Glacier Perito Moreno (GPM) in southern Patagonia, Argentina. The system continuously monitors glacier front evolution during daylight hours with a subdaily temporal resolution of $30\,\mathrm{min}$, while a 4G connection enables near-real-time analysis and supports the capture of rapid calving dynamics. Its design enables fully autonomous operation and data transfer, providing time-lapse imagery with partially overlapping views of the glacier front for subsequent 4D point cloud reconstruction using a Structure from Motion Multi-View Stereo (SfM-MVS) workflow. The resulting point clouds are compared between successive epochs using Multiscale Model to Model Cloud Comparison (M3C2) approach (Lague et al., 2013) to quantify changes in calving evolution. This framework is intended to support long-term calving analysis and future forecasting research, as well as the identification of potential key calving factors.

Installing a multi-camera monitoring system in challenging environments, such as a glacier, requires robust protection of all components; however, despite these precautions, adverse conditions such as water droplets or moisture often degrade image quality. Moreover, glacier dynamics, such as continuous motion, can affect the reliability of point cloud comparisons. Neglecting these aspects can lead to reduced image correlation, which in turn impairs bundle adjustment and point cloud precision. While the first issue can be mitigated through appropriate image pre-processing (Guidi et al., 2014) or by filtering out low-quality images, the second can be addressed using an advanced SfM-MVS method called Multi-Epoch Multi-Imagery (MEMI). This approach extends standard SfM-MVS by jointly processing images from two consecutive epochs, with multiple images acquired from each camera position at each epoch. During image alignment and bundle adjustment (hereafter referred to as the alignment-adjustment process), all images are processed together to jointly estimate the camera parameters based on tie points detected across epochs, forming a joint sparse point cloud. Using these estimated parameters, georeferenced

This contribution has been peer-reviewed. The double-blind peer-review was conducted on the basis of the full paper.
https://doi.org/10.5194/isprs-annals-XI-2-2026-615-2026

dense point clouds can be generated separately from the image bursts of each temporal epoch, t1 and t2 (Figure 1).

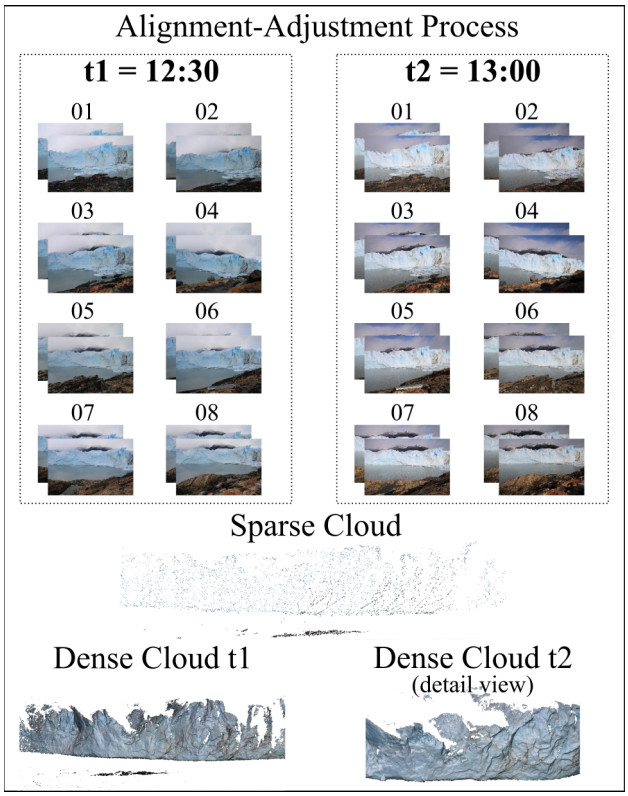

Figure 1. Schematic of model reconstruction using Multi-Epoch Multi-Imagery (MEMI) time-lapse photogrammetry.

The advantages of the MEMI approach lie in the redundancy of its observations, which increases the reliability of the estimated camera parameters. On the one hand, when observations of two epochs are considered, spatially correlated systematic errors are introduced consistently during dense cloud generation, helping to mitigate systematic alignment errors in change detection after point-cloud differencing. On the other hand, the use of multi-imagery within each epoch increases image redundancy and improves tie point quality, as demonstrated by (Blanch et al., 2021) and (Hollander et al., 2025) for unchanged scenes, where significant improvements are achieved compared with the previous multi-epoch single-imagery approach (Feurer and Vinatier, 2018). Together, these aspects lead to improved model quality, while alignment across epochs ensures shared homologous points and a consistent camera geometry reconstruction. As a result, the relative accuracy of point-cloud differencing is improved, which becomes particularly evident when compared with a classic SfM-MVS workflow, in which camera parameters are estimated independently for each epoch, potentially leading to inconsistencies in the reconstructed geometry that affect subsequent comparison. Therefore, as MEMI surpasses previous methods, it has been implemented and further developed for the highly dynamic dataset presented in this study.

The remainder of this paper is structured as follows: First, the study area and equipment are described, followed by the workflow pipeline for automated 4D point cloud generation. This includes data acquisition and transfer, image pre-processing, and, as the focus of this study, the MEMI processing, outlining the main challenges to be overcome. The subsequent section presents results based on a representative eight-day subset period, evaluating the effect of varying MEMI parameters on computational efficiency and alignment accuracy. To demonstrate the potential of the MEMI approach, an example of pre-failure calving deformation and multiple estimates of calving retreat magnitude are presented. Finally, conclusions and an outlook on ongoing research are given.

2. Study Area and Equipment

The lake-terminating GPM is one of the glaciers that form part of the Southern Patagonian Icefield (SPI) and is located within Los Glaciares National Park, in the province of Santa Cruz, Argentina. This glacier has a length of about 30 km and according to (Lenzano et al., 2018), was characterized by its unusual behavior, exhibiting only minor fluctuations of the glacier front. Since the installation of the multi-cameras system in December 2024, this situation has changed. The RGB cameras have recorded a retreat of the GPM, which, at the time of installation, occupied around 30 % of the field of view (FOV) (Figure 2).

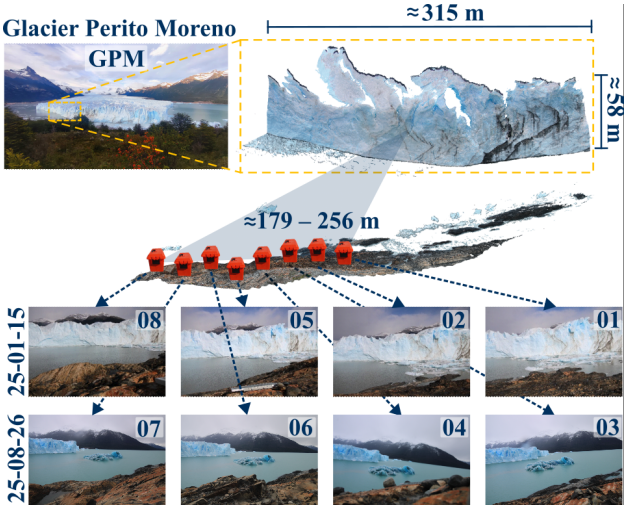

Figure 2. 3D point cloud of the GPM front showing the locations of camera systems and their fields of view on two different days.

Each of the eight systems are protected by stable housing and consists of following components:

- A commercial DSLR camera (Canon EOS 2000D; image resolution 6000×4000 pixel (px), pixel size 3.72 µm) used for RGB glacier imaging and equipped with a zoom lens.
- A single-board computer (SBC) (Raspberry Pi 3 Model B+) with a Witty Pi Real Time Clock (RTC) shield.
- A router (Teltonika RUT200) providing 4G connectivity for near-real-time analysis.
- A 128 GB USB drive for backup storage.
- A 12 V, 24 Ah AGM battery.
- A 30 W solar panel.

The SBC is responsible for battery scheduling, data acquisition (images and logs), and data transfer (Section 3.1). The transferred data are subsequently pre-processed and processed through a fully automated MEMI workflow on a workstation equipped with a 13th Gen Intel® Core™ i9-13900K processor (24 cores, 32 threads), 128 GB of RAM, and an NVIDIA GeForce RTX 3070 GPU.

https://doi.org/10.5194/isprs-annals-XI-2-2026-615-2026

3. Automated 4D Point Cloud Generation

Data processing for automated 4D point cloud reconstruction is outlined in Figure 3. The workflow comprises data acquisition and transmission, image pre-processing, and automated SfM-MVS processing. Given the large data volume and continuous data acquisition, all processes are designed for automated execution. In this study, emphasis is placed on the MEMI processing applied successively to all acquired epochs to generate a robust and consistent point cloud sequence. The resulting 4D point clouds form the basis for developing a calving deformation inventory to support future AI-based forecasting analyses.

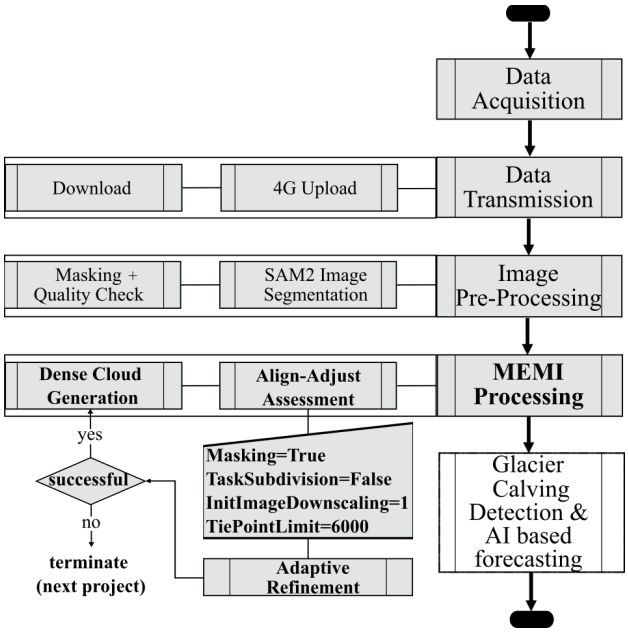

Figure 3. 4D point cloud generation workflow highlighting MEMI processing; the parallelogram denotes the reference parameter configuration.

3.1 Data Acquisition

Using the monitoring system described in Section 2, images with manually set focus and automatically controlled exposure time are captured by the cameras at a sub-daily frequency of every $30\,\mathrm{min}$. The duration of daily acquisitions varies seasonally with solar elevation. On the shortest and longest days (21 June and 21 December), the number of daily captures ranges from 16 to 33, respectively. To ensure multi-imagery for the subsequent processing, each camera captures two consecutive images per epoch, resulting in 256 to 530 images per day, providing all systems operate correctly.

For the initial estimation of internal and external camera calibration parameters, additional images of the glacier wall were acquired under stable weather and surface conditions. These images were captured using a DJI Mavic 3 Enterprise drone with PPK-GNSS positioning and two additional hand-held DSLR cameras along the transect of the eight fixed systems. The resulting dense cloud is shown in Figure 2, with the derived camera parameters serving as initial values for each MEMI processing. However, to account for temperature-related variations, the focal length and principal point can be adjusted within each iteration.

Finally, georeferencing could not be performed using standard Ground Control Points (GCPs), as no stable surfaces are available directly in front of the cameras. The systems are positioned substantially above the rock shore, and potential GCP sites are either below the FOV, periodically submerged, or not visible to multiple cameras. Consequently, the positions of the camera systems were measured with a mobile GNSS receiver and used as direct georeferencing (James et al., 2017) for the camera parameter estimation described above. The resulting adjusted camera coordinates, with centimeter-level accuracy, are then used as initial coordinates in each MEMI processing. While this approach could introduce an unknown absolute positional offset, its influence on point cloud differencing is negligible, as the offset is systematic across epochs and therefore cancels out in relative change detection.

3.2 Data Transmission

The acquired images in JPG format and daily logs are stored on local USB drives and uploaded twice daily via a 4G connection to Google Drive. The uploaded data are subsequently downloaded once daily to the workstation. Data transfer reliability depends on 4G network availability and local access conditions in the National Park, which results in temporal gaps in the downloaded image record. These gaps are primarily caused by limited 4G connectivity and do not indicate data loss, as images that are not uploaded remain stored on the local USB drives. As of 27 March 2026, the missing data have been retrieved to the workstation during two maintenance visits since installation, and multi-imagery for a total of 6,878 epochs has been collected for SfM-MVS analysis.

3.3 Image Pre-Processing

Pre-processing is applied to the acquired images to improve quality checking and reduce ambiguities during image correlation. As illustrated in Figure 4, which shows examples of environmental and scene conditions affecting image contrast, the glacier wall is surrounded by a lake, mountains (seasonally covered by snow), and the sky. In certain situations, such as when clouds cover parts of the glacier, or when ice blocks float on the lake, the success of image correlation decreases due to the presence of similar adjacent textures and dynamically changing regions.

To check image quality, blur metrics such as the Laplacian or Sobel indicators are often used (Rajabli, 2025, Blanch et al., 2021). However, because these metrics quantify texture contrast based on pixel-value variability, and the observed scene is generally weakly textured and exhibits low radiometric contrast, their resulting values may not reliably represent true contrast. As a consequence, defining a threshold that consistently distinguishes low-quality images is difficult.

Isolating relevant image regions through masking may therefore enhance the sensitivity of quality metrics and reduce ambiguity during image correlation. Masking the sky, mountains, and lake minimizes the influence of surrounding regions with low texture quality or instability. Likewise, keeping the rock shore unmasked ensures that the MEMI process includes sufficiently stable areas within the FOV of the cameras in both epochs, a requirement for reliable processing (Blanch et al., 2021) given continuous glacier motion. In addition, assessing image quality only on the unmasked regions yields clearer blur metrics than when evaluating the whole image (Figure 5), thereby indicating whether the regions of interest exhibit low contrast.

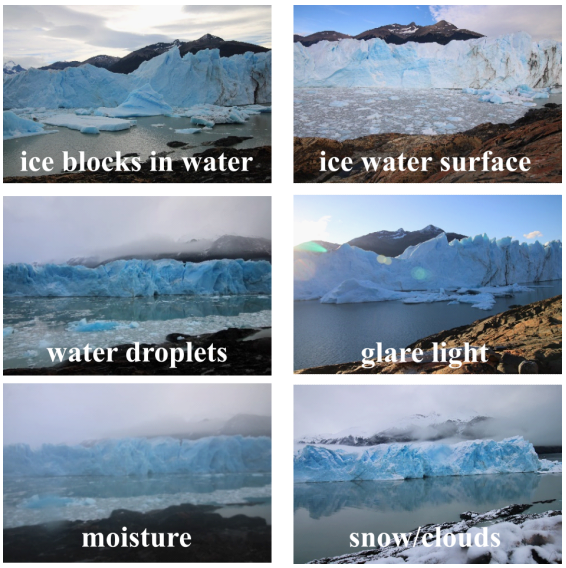

Figure 4. Examples of dynamic scene and environmental factors that reduce image contrast and correlation success.

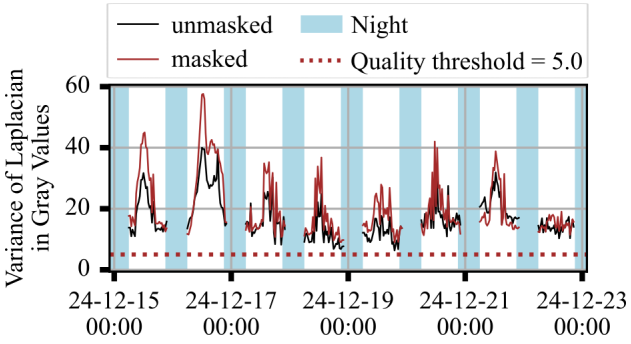

Figure 5. Quality metrics for masked/unmasked images from 1 Multi-View Stereo system with an empirical quality threshold over eight days.

Given the large number of collected images and the absence of GCPs for adaptively updating masked areas, as in (Blanch et al., 2021), (Nagathihalli Lokesh et al., 2025) further developed the AI-based image segmentation model SAM2 and applied it to the dataset presented here. Interestingly, the segmentation performance was more affected by strong illumination changes than by adverse conditions such as clouds or water droplets. Therefore, after the initial masking, further refinement of the glacier and rock shore areas is performed when needed (Figure 6) using the Intersection-over-Union (IoU) values from the temporally closest, best-segmented epoch. The IoU values serve as a confidence measure of segmentation reliability, and an empirically defined class value acceptance of $IoU_{img,cls} \geq \overline{IoU}cls - 0.2 \times \sigma IoU_{cls}$ is applied. Regardless of whether IoU refinement is required, a morphological dilation to the masked areas is applied, yielding consistent and reliable results. The influence of masking on alignment-adjustment performance is evaluated as a test parameter in the subsequent MEMI processing.

3.4 MEMI Processing

During implementation of the MEMI workflow, several challenges were identified. These include (i) ensuring a reliable

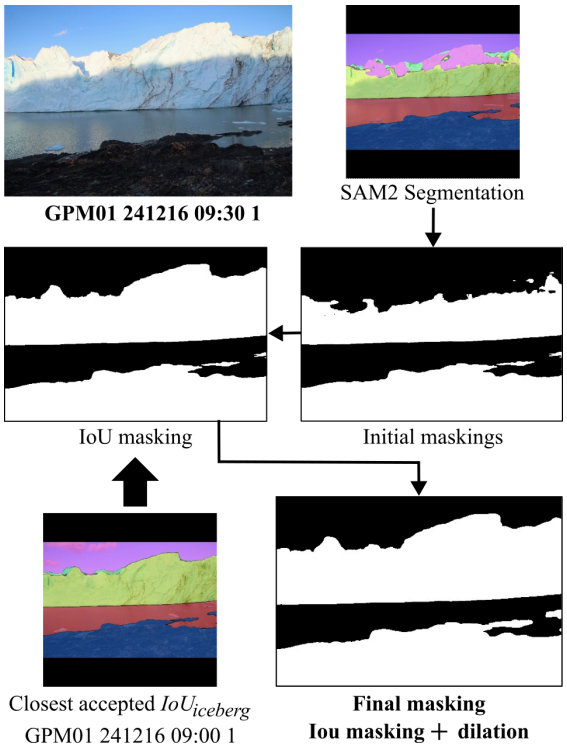

Figure 6. IoU-based segmentation for optimized image masks.

image pre-processing procedure (Section 3.3) to prevent processing failures caused by controllable image issues, and (ii) developing a robust strategy and parameter configuration for optimized alignment-adjustment processing, as addressed in the following subsections.

The evaluation of image quality and alignment-adjustment optimization aim to meet two main performance objectives:

1. **Minimized processing time**, given that two point clouds can theoretically be generated for each of the 6,878 processing projects (Section 3.2).
2. **Highest possible tie point accuracy ($<$ 1 px)**, to ensure optimal alignment accuracy and point-cloud precision for successful calving-detection analysis.

To meet these objectives, poor-quality images are automatically discarded to prevent degradation of correlation results and to reduce processing time, while alignment-adjustment parameters are optimized and adaptively refined for robust sparse point cloud generation. With respect to the alignment-adjustment, parameters that are systematically varied, including masking, are presented in Section 3.4.1 to define configuration sets for optimizing the tie point computation strategy. These configuration sets define initial alignment-adjustment parameters, which are subsequently refined through the adaptive refinement procedure, as described in Section 3.4.2, resulting in final parameters suitable for varying image quality across epochs. This approach aims to enhance the precision of the sparse point clouds and, when the refinement leads to a successful alignment-adjustment assessment, dense point clouds are generated (Figure 3). The processing steps are implemented in (Agisoft Metashape Professional, 2025) (version 2.2.0) and automated via the available Python API (version 3.10.11) (Python Software Foundation, 2023).

3.4.1 Parameter Testing for Alignment-Adjustment Optimization In addition to whether masking unstable regions is applied, further alignment-adjustment parameters are evaluated to balance computational efficiency with acceptable $TiePoints_{RMSE}$ values and consistent dense cloud generation across epochs. The tested parameters correspond to variations of the reference configuration listed in Figure 3 and were selected according to their descriptions in (Agisoft LLC, 2025):

- *TaskSubdivision=True*, for faster alignment-adjustment processing;
- *InitImageDownscaling=0*, to improve the localization of tie points and the estimation of camera positions; and
- *TiePointLimit=0*, to disable tie point filtering and obtain as many tie points as possible.

The variation of these parameters results in the configuration sets summarized in Table 1, which define part of the initial alignment-adjustment parameters used for the subsequent adaptive refinement.

SETS	Task Subdivision	InitImage Scaling	Masking	TiePoint Limit
SET1	False	1	True	6000
SET2	False	1	False	6000
SET3	False	1	True	0
SET4	False	0	True	6000
SET5	True	1	True	6000

Table 1. Configuration sets used to evaluate MEMI performance.

3.4.2 Adaptive Refinement The aim of the iterative refinement of the tie point computation is to maximize the number of valid models that satisfy two conditions evaluated throughout the process: a minimum number of tie points ($\mathbf{TiePoints_{num} \geq 3500}$) and an acceptable tie point accuracy ($\mathbf{TiePoints_{RMSE} \leq 1\,px}$). To achieve this, the refinement approaches implemented in (Blanch et al., 2021) and (Grothum et al., 2025) are employed in the refinement procedure presented in Figure 7.

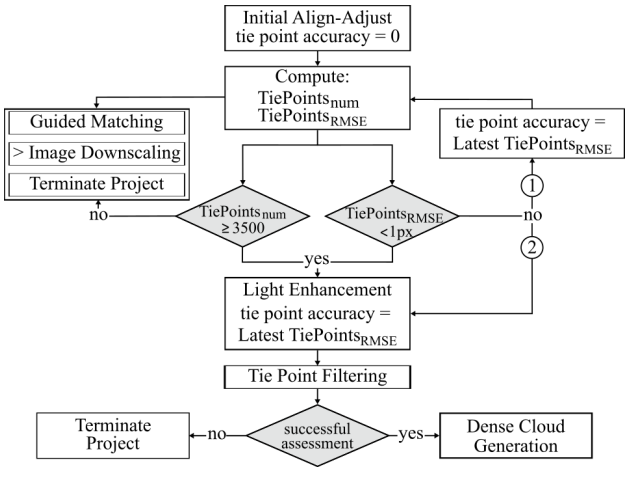

Figure 7. Adaptive refinement procedure for alignment-adjustment prior to dense cloud generation.

The workflow begins with an initial alignment-adjustment, after which the resulting $\mathbf{TiePoints_{num}}$ and $\mathbf{TiePoints_{RMSE}}$ are evaluated. If the minimum tie point number is not achieved, feature matching is iteratively improved through guided matching and image downscaling, whereas insufficient tie point accuracy leads to re-estimation using the latest RMSE (James et al., 2017). Following this, a final light enhancement and tie point filtering are applied. If the assessment is successful, dense point cloud generation is performed; otherwise, the processing is terminated.

4. Performance Assessment of MEMI Processing

The configuration sets in Table 1 were evaluated over an eight-day period in December 2024 to assess their effect on processing performance. The results focus on the trade-off between computational efficiency and alignment-adjustment accuracy, as summarized in Section 4.1, followed by an analysis of masking effects on calving detection reliability (Section 4.2). Based on the selected configuration set, a daily seasonal behavior of the computed tie point cloud models is then presented (Section 4.3), and an initial estimation of calving magnitudes for this period is provided (Section 4.4).

4.1 Performance Findings

The comparison of configuration sets indicates that differences in performance are primarily expressed in computational efficiency and robustness, while alignment-adjustment accuracy remains broadly consistent across all configurations. As shown in Figure 8, $\boldsymbol{TiePoints_{RMSE}}$ values vary only marginally between configurations over the eight-day period, with no systematic degradation in accuracy, highlighting the effectiveness of the adaptive refinement procedure. This consistency is further supported by the median values reported in Table 2, confirming that all configurations achieve comparable geometric alignment-adjustment despite differences in tie point computation strategies.

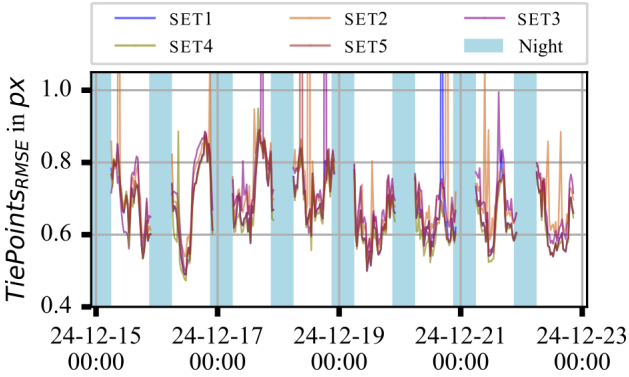

Figure 8. Alignment accuracy measured by $\boldsymbol{TiePoints_{RMSE}}$ for SET1-SET5 over eight days.

SETS	Failed Projects	TiePoints RMSE (median)	Iter. Align-Adjust (iter/ocurr/num)
SET1	1/260	0.66	4 / 38/ 260
SET2	5/260	0.69	4 /119/ 260
SET3	2/260	0.70	4 / 49/ 260
SET4	0/260	0.64	4 / 33/ 260
SET5	1/260	0.66	4 / 36/ 260

Table 2. Performance summary of alignment accuracy for each SET. Iterative Alignment-Adjustment is given as *iterations / occurrences / totalProjects*, where occurrences is the count of projects with that maximum number of iterations.

However, the impact of masking on performance is clearly reflected in both model robustness and computational efficiency. The configuration without masking (SET2) shows the highest number of failed projects and the most frequent occurrence of four adaptive refinements (Table 2), indicating reduced stability under dynamic scene conditions. These effects are also visible in the dense point cloud density (Figure 9), where fluctuations coincide with epochs affected by floating ice and changing illumination, particularly around December 21. Although SET2 achieves relatively lower alignment-adjustment times (Table 3), this does not translate into improved overall efficiency, as less reliable alignment parameters negatively affect subsequent dense reconstruction.

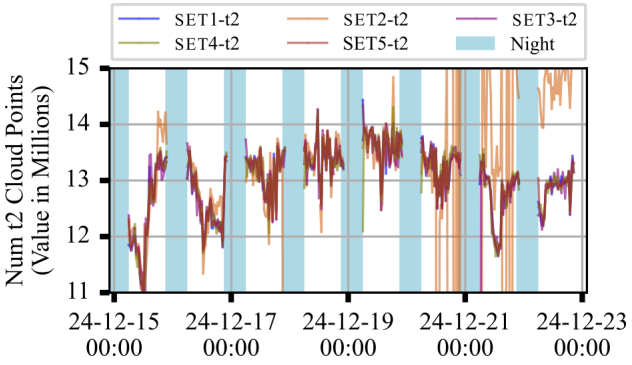

Figure 9. Dense point cloud density for the second epoch (t2) in each processing project over eight days.

SETS	Project Duration (median)	Align-Adjust (median)	Dense Cloud Generation (median)
SET1	9 min 18 s	1 min 12 s	7 min 37 s
SET2	10 min 2 s	1 min 9 s	8 min 26 s
SET3	10 min 24 s	2 min 6 s	7 min 48 s
SET4	9 min 38 s	1 min 18 s	7 min 53 s
SET5	9 min 40 s	1 min 22 s	7 min 50 s

Table 3. Performance summary of computer efficiency for each SET using medians.

Configurations incorporating masking demonstrate more stable performance, with fewer failures and more consistent alignment-adjustment behavior, as well as comparable dense point cloud densities. Among these, SET4 consistently achieves the lowest median $\boldsymbol{TiePoints}_{RMSE}$, the fewest refinement iterations, and no failed projects, suggesting that image upscaling, although undocumented in (Agisoft LLC, 2025), improves tie point reliability and model robustness. Therefore, using the highest image scaling ($= \mathbf{0}$) may be advantageous, with a moderate increase in project duration.

Finally, differences between masked configurations are mainly related to efficiency trade-offs rather than accuracy. For example, SET3 increases alignment-adjustment time without clear gains in tie point accuracy, as all available matching points are used for model parameter estimation. In addition, SET5 introduces additional computational overhead due to task subdivision, which proves not beneficial for small image sets (32 images per project). In contrast, SET1 provides the lowest overall project duration while maintaining stable alignment and reconstruction performance, representing the most balanced configuration.

4.2 Effect of Masking on Calving Detection

While the lack of masking shows a moderate negative effect compared with the use of masking, it may become more challenging for point-cloud differencing, where unreliable points may compromise calving deformation and failure detection. An example is shown in Figure 10, where M3C2 was applied to dense clouds from the same epochs processed using SET1 and SET2 with (CloudCompare, 2025), including a dense cloud overlay and image crops from both epochs highlighting the affected areas. Prior to M3C2 computation, identical cleaning procedures were applied to both point clouds, and a core point diameter of 0.4 m was used to better capture deformation.

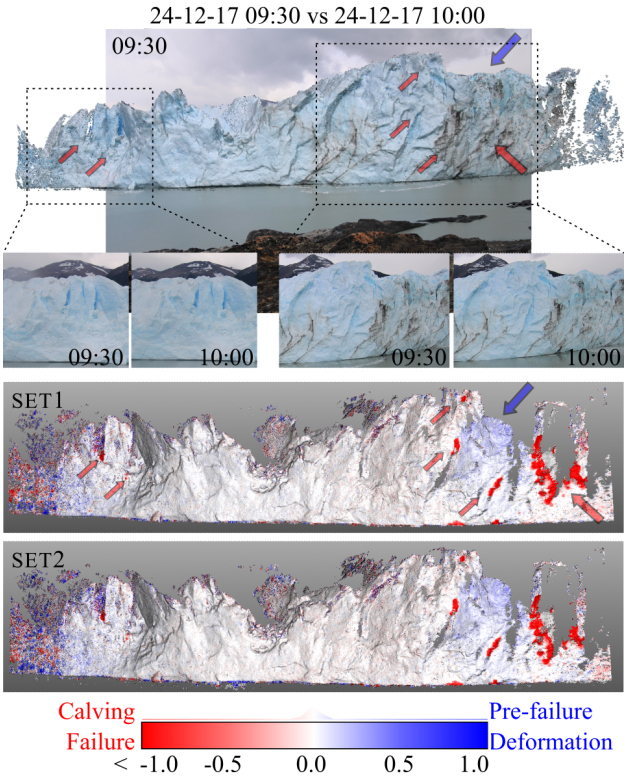

Figure 10. M3C2 comparison between SET1 and SET2 for the same epochs, including dense cloud overlay and image crops from both epochs highlighting calving failures (red arrows) and pre-failure deformation (blue arrow).

The calving failures in SET1 (red arrows) appear marginally sharper, and the pre-failure deformation surface (blue arrow) is more pronounced. Implementing analyses described in (Lague et al., 2013) suggests that these differences result from SET1 achieving a slightly higher proportion of significant change points (74.54 % vs. 74.28 %) and a larger share of significant points with Level of Detection (LoD) below 0.05 m (89.15 % vs. 88.05 %), considering both positive and negative changes, as well as a higher proportion of significant positive distances (46.03% vs. 42.71%), indicating more reliable detection of pre-failure deformation. Visually, the M3C2 results for SET1 appear less noisy, with more homogeneous distances over stable glacier areas.

Note that the remaining red and blue areas not marked by arrows result from the small color scale used to display pre-failure deformation. This visualization also highlights the importance of precise point clouds and robust LoD analyses for the reliable detection of pre-failure deformation in calving areas.

This contribution has been peer-reviewed. The double-blind peer-review was conducted on the basis of the full paper.
https://doi.org/10.5194/isprs-annals-XI-2-2026-615-2026 | © Author(s) 2026. CC BY 4.0 License.

4.3 Daily Seasonality

A distinct daily seasonality was already evident in the alignment accuracy results shown in Figure 8. This pattern becomes even more apparent when different times of day are highlighted, as presented for the SET1 alignment assessment in Figure 11, including representative image pairs (one image per epoch) illustrating cases of low and high accuracy. In general, $\boldsymbol{TiePoints_{RMSE}}$ values are higher in the morning, decrease toward midday, increase again in the afternoon, and drop at night. This pattern is inversely related to $\boldsymbol{TiePoints_{num}}$, which peaks at midday and decreases in the afternoon. These results indicate a strong influence of sunlight, as the best alignment is achieved when the sun is near its zenith and the poorest when images are captured against the light in the afternoon. It is also noteworthy that $\boldsymbol{TiePoints_{num}}$ values are higher at the beginning of the day, while $\boldsymbol{TiePoints_{RMSE}}$ is not at its minimum. These values result from the processing between epochs of two consecutive days. Although this pattern differs from the general daily trend, it demonstrates that MEMI can still achieve robust alignment even when the position of the glacier has changed significantly. This positional change likely causes the higher morning $\boldsymbol{TiePoints_{RMSE}}$, whereas the higher $\boldsymbol{TiePoints_{num}}$ result from the low sun behind the cameras, which illuminates the scene and enhances visible texture, thereby facilitating point matching.

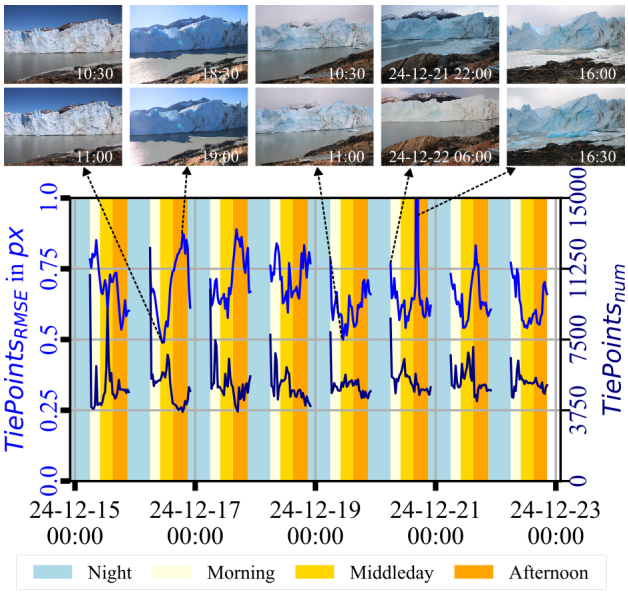

Figure 11. Daily seasonality of $\boldsymbol{TiePoints_{RMSE}}$ and $\boldsymbol{TiePoints_{num}}$ for SET1 over eight days.

Although alignment accuracy varies throughout the day, it remains within the acceptable range (Section 3.4.2) and does not affect overall processing performance. Within the analyzed period, no significant influence of changing light or weather conditions is observed. As reported in Section 4.1, only one project failed, and no clear seasonal trend is evident in the reconstructed dense point density.

4.4 Calving Magnitude Estimation

To demonstrate the potential of the MEMI approach, estimates of calving failure events based on significant (i.e., above LoD) M3C2 distances derived from dense point-cloud differencing at 30 min intervals are presented in Figure 12. The vertical axis shows the daily cumulative calving magnitudes for the eight days of the analysis period. These magnitudes represent retreat distances inferred from M3C2 distances and do not correspond to volumetric estimates of calving events. Calving magnitude was approximated using the lower tail of a Gaussian fit to the histogram of significant M3C2 distances, where the lower bound ($\mu - 4\sigma$) provides a conservative estimate of maximum retreat and reduces the underestimation of large calving events.

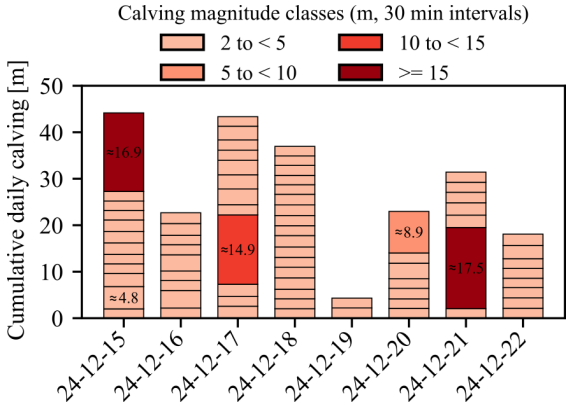

Figure 12. Calving magnitudes derived from significant M3C2 distances between successive dense point clouds.

During this period, numerous small-scale retreat magnitudes between 2 m and 5 m are observed, while the largest events (∼17.5 m) affect nearly the entire glacier wall (between 30 m to 55 m). Distances below 2 m are excluded, as the lower-bound approach may overestimate calving in this range due to μ being close to 0, where the values may fall within the point cloud differencing error. This highlights the challenge of distinguishing measurement uncertainty, small calving events, and pre-failure deformation within small-magnitude ranges.

5. Conclusion and Outlook

Generating an automated 4D point cloud model sequence for monitoring the lake-terminating Glacier Perito Moreno with a multi-camera system for SfM-MVS processing is challenging due to the dynamic behavior of the glacier and harsh environmental conditions affecting image quality. The optimized and automated Multi-Epoch Multi-Imagery workflow developed in this study addresses these issues through daily image acquisition, masking of unstable regions, and adaptive refinement of alignment-adjustment parameters. These improvements enabled the generation of precise point clouds for most epochs within the eight-day period analyzed, providing a reliable basis for point cloud differencing and calving analyses.

The configuration sets tested in this study were designed to identify the best-performing processing pipeline in terms of computational efficiency, robustness, and alignment accuracy. While alignment-adjustment accuracy remained largely consistent across configurations, performance differences were primarily expressed in computational efficiency and robustness. In particular, masking proved essential under dynamic scene conditions, as unmasked configurations exhibited increased failure rates, reduced dense cloud consistency, and impaired detection of subtle deformation processes.

Overall, the enhanced MEMI workflow demonstrated its capability for generating a comprehensive calving inventory during

the summer period. However, as the season progresses toward late summer, environmental conditions increasingly affect image quality, leading to a higher frequency of failed alignment-adjustment assessments. Future work will test the approach under remaining seasonal conditions and integrate thermal infrared imagery for nighttime monitoring. Incorporating additional environmental parameters, such as solar radiation and temperature, will support AI-based calving forecasting, improve understanding of key drivers of glacier calving, and help explain variability in retreat magnitudes.

Acknowledgements

This research was funded by the Deutsche Forschungsgemeinschaft (DFG, German Research Foundation) through the projects “AI4Glaciers” (project no. 536233846) and “SFB/TRR 280” (project no. 417002380). We thank Steffen Welsch for his support in installing and maintaining the monitoring systems and for logistical assistance in the field.

References

Agisoft LLC, 2025. Agisoft Metashape user manual – professional edition, version 2.2. https://www.agisoft.com/downloads/user-manuals/.

Agisoft Metashape Professional, 2025. How to Install Metashape Stand-alone Python Module, Version 2.2.0. Agisoft Helpdesk Portal, https://agisoft.freshdesk.com/support/solutions/articles/31000148930-how-to-install-metashape-stand-alone-python-module. Last modified: 3 September 2025. Accessed on 11 February 2025.

Anders, K., Winiwarter, L., Höfle, B., 2022. Improving Change Analysis From Near-Continuous 3D Time Series by Considering Full Temporal Information. *IEEE Geoscience and Remote Sensing Letters*, 19, 1–5. https://ieeexplore.ieee.org/document/9702133/.

Blanch, X., Eltner, A., Guinau, M., Abellan, A., 2021. Multi-Epoch and Multi-Imagery (MEMI) Photogrammetric Workflow for Enhanced Change Detection Using Time-Lapse Cameras. *Remote Sensing*, 13(8). https://www.mdpi.com/2072-4292/13/8/1460. Number: 8 Publisher: Multidisciplinary Digital Publishing Institute.

Blanch, X., Guinau, M., Eltner, A., Abellan, A., 2023. Fixed photogrammetric systems for natural hazard monitoring with high spatio-temporal resolution. *Natural Hazards and Earth System Sciences*, 23(10), 3285–3303. https://nhess.copernicus.org/articles/23/3285/2023/. Publisher: Copernicus GmbH.

CloudCompare, 2025. CloudCompare (Version 2.12.4). https://www.cloudcompare.org/. Accessed on 16 March 2023.

Eltner, A., Kaiser, A., Abellan, A., Schindewolf, M., 2017. Time lapse structure-from-motion photogrammetry for continuous geomorphic monitoring. *Earth Surface Processes and Landforms*, 42(14), 2240–2253. https://onlinelibrary.wiley.com/doi/abs/10.1002/esp.4178.

Feurer, D., Vinatier, F., 2018. Joining multi-epoch archival aerial images in a single SfM block allows 3-D change detection with almost exclusively image information. *ISPRS Journal of Photogrammetry and Remote Sensing*, 146, 495–506. https://linkinghub.elsevier.com/retrieve/pii/S0924271618302946.

Grothum, O., Epple, L., Bienert, A., Blanch, X., Eltner, A., 2025. Near-continuous observation of soil surface changes at single slopes with high spatial resolution via an automated SfM photogrammetric mapping approach. *SOIL*, 11(2), 1007–1028. https://soil.copernicus.org/articles/11/1007/2025/.

Guidi, G., Gonizzi, S., Micoli, L.L., 2014. Image preprocessing for optimizing automated photogrammetry performances. *ISPRS Annals of the Photogrammetry, Remote Sensing and Spatial Information Sciences*, II-5, 145–152. https://isprs-annals.copernicus.org/articles/II-5/145/2014/isprsannals-II-5-145-2014.html. Conference Name: ISPRS Technical Commission V Symposium (Volume II-5) - 23–25 June 2014, Riva del Garda, Italy Publisher: Copernicus GmbH.

Hollander, J., Kromer, R., Walton, G., 2025. Development of a Rockfall Database with Fixed Photogrammetry: Comparison of the Multi-epoch and Multi-imagery Method to Classical Structure-from-Motion Workflows and Evaluation of Rockfall Seasonality. *Rock Mechanics and Rock Engineering*. https://doi.org/10.1007/s00603-025-04824-x.

James, M. R., Robson, S., Smith, M. W., 2017. 3-D uncertainty-based topographic change detection with structure-from-motion photogrammetry: precision maps for ground control and directly georeferenced surveys. *Earth Surface Processes and Landforms*, 42(12), 1769–1788. https://onlinelibrary.wiley.com/doi/abs/10.1002/esp.4125.

Lague, D., Brodu, N., Leroux, J., 2013. Accurate 3D comparison of complex topography with terrestrial laser scanner: Application to the Rangitikei canyon (N-Z). *ISPRS Journal of Photogrammetry and Remote Sensing*, 82, 10–26. https://linkinghub.elsevier.com/retrieve/pii/S0924271613001184.

Lenzano, M. G., Lannutti, E., Toth, C., Lenzano, L., Lo Vecchio, A., Falaschi, D., Vich, A., 2018. Analyzing the oscillations of the Perito Moreno Glacier, using time-lapse image sequences. *Cold Regions Science and Technology*, 146, 155–166. https://www.sciencedirect.com/science/article/pii/S0165232X17304238.

Nagathihalli Lokesh, B., Duran Vergara, L., Mass, H.-G., Eltner, A., 2025. Evaluating the Adaptation Potential of SAM2 for Glacier Segmentation in Severe Weather. *ISPRS Journal of Photogrammetry and Remote Sensing*, 1–5. Abstract Submitted on November 2025.

Python Software Foundation, 2023. Python Release: Python 3.10.11. https://www.python.org/downloads/release/python-31011/. Released on 5 April 2023. Accessed on 27 February 2025.

Rajabli, A., 2025. How can you tell whether this image is blurry? https://medium.com/@ayselrajabli/how-can-you-tell-whether-this-image-is-blurry-ce152ef11ed8. Accessed: October 2025.

The GlaMBIE Team, 2025. Community estimate of global glacier mass changes from 2000 to 2023. *Nature*, 639(8054), 382–388. https://www.nature.com/articles/s41586-024-08545-z. Publisher: Nature Publishing Group.

Ulm, M., Elias, M., Eltner, A., Lotsari, E., Anders, K., 2025. Automated change detection in photogrammetric 4D point clouds – transferability and extension of 4D objects-by-change for monitoring riverbank dynamics using low-cost cameras. *Applied Geomatics*, 17(2), 367–378. https://doi.org/10.1007/s12518-025-00623-9.